Multi-scale Biophysical Principles in Clinical Irreversible Electroporation

Daniel C. Sweeney, Robert E. Neal II, and Rafael V. Davalos

3.1   Introduction

Irreversible electroporation (IRE) is a focal ablation methodology that involves generating brief, but intense, electric fields in a target tissue. These electric fields operate on the cell level to electrically perforate—or permeabilize—the cell membrane while maintaining the structural integrity of the extracellular components [12]. The development of IRE technology significantly improved the outcomes of patients with late-stage pancreatic cancer. A study investigating such outcomes found that the median survival of stage III pancreatic cancer patients rose from 6–13 to 24.9 months in a 200-person study following IRE treatment [31], roughly doubling patient post-treatment survival.

The movement of electrons and other charged moieties is central to the mechanisms driving the clinical efficacy of IRE, which are motivated by an electrical potential (voltage) gradient. Similar to heat conduction, such a gradient is usually established using one electrode/s from which the electrons flow (source) and one or more electrode that accept the flow of electrodes (sinks). The geometry of the source and sink electrodes largely determine the distribution of electric field within a target tissue during an IRE procedure. It is imperative that the clinician has a conceptual understanding of how electric fields are distributed when treating a patient with IRE, and we seek to provide the context and intuitive understanding of the phenomena motiving IRE treatment in this chapter.

One of the central considerations inherent in any procedure involving the application of electric fields is that they are difficult to visualize in real time. Visualization

D.C. Sweeney (✉) • R.V. Davalos
Department of Biomedical Engineering and Mechanics, Virginia Tech,
330 Kelly Hall, Blacksburg, VA, USA
e-mail: sweeneyd@vt.edu

R.E. Neal II
Angio Dynamics Inc., Queensbury, NY, USA

is difficult for any electric field distribution because it represents the force that can be exerted on a unit electrical charge positioned at every point. For the case of the electric fields generated in IRE procedures, these fields represent the force acting on a charged particle, rather than the movement of the particle itself, and therefore may only be evaluated indirectly. While monitoring electron flow [27] and the small changes in temperature generated during IRE [5], clinicians have largely relied on treatment planning algorithms and empirical or a priori knowledge of the tumor anatomy and physiology to determine the order in which ablations should occur and their positioning within the tissue to optimally destroy the target tissue while minimizing collateral damage to healthy tissue.

Several mathematical techniques form the foundation for the clinically relevant treatment planning for IRE procedures. Analytical techniques are useful for gaining an intuitive understanding of the biophysical mechanisms associated with IRE. These techniques, however, are not able to capture many of the geometric complexities of biological tissue and have little clinical use outside of gaining a clinical intuition about how electric fields behave in such materials. Analytical techniques will be discussed at the cellular level, and, while not explicitly accurate for every example, it is our hope that the conceptual lessons learned from these mathematical formulations will give the reader an intuitive understanding of why and how IRE is performed the way it is.

The finite element method (FEM) is the workhorse of IRE treatment planning and will be utilized to outline the tissue-level considerations in the second part of this chapter. In IRE procedures, FEM modeling is especially useful because real, patient-specific tumor, organ, and tissue geometries are used to plan individual- and tumor-specific ablations. In a typical model, images from 3-D medical imaging modalities—such as MRI or CT scans—are reconstructed into 3-D geometries and then subdivided into smaller sections or finite elements. The governing physical principles are then solved on each element. These elements are then used to reconstruct piecewise functions that allow the relevant physical quantities to be determined at every point within the whole geometry. For example, in a typical IRE procedure, a clinician might image a tumor and send the scans to an engineer who will reconstruct the scans into their 3-D geometries. Once reconstructed, the engineer will insert models of electrodes into the tissue and determine how the electric field should be applied to which electrodes in which order for optimal tissue ablation [16]. The engineer will send the reconstructed model back to the clinician prior to treatment so that they are able to perform the treatment in the optimal manner.

3.2 Electric Fields

Electromagnetic fields appear ubiquitously throughout the biological realm; chemical gradients directly give rise to electric fields, appearing in fields from developmental biology to wound healing. Modern electrodynamic theory was developed by James Clerk Maxwell in the mid-nineteenth century [32] and has subsequently been adapted and developed to explain electrical phenomena observed in biological interactions.

Within a tissue, the local electric field intensity is directly related to the ablation field [12]. If modeled accurately, it can provide invaluable information to the medical operator toward the visualization of the expected final lesion volume and how it will change in relation to adjusting ablation parameters (geometry, pulse number, length, voltage, etc.). Therefore, the assumptions, considerations, and solutions critical to mathematically modeling electroporation are developed below with the goals of compiling and reviewing the essential concepts that have driven the advancement of electroporation.

3.2.1 Pulse Characteristics

The electric fields generated for clinical use have included many different wave shapes, including triangular, ramp, sinusoidal, and exponential, though typically treatments are delivered using square pulses. However, typically square pulses are used for IRE treatment, and it is important to discuss the terminology associated with such waveforms before delving into the physical concepts relevant to IRE. Figure 3.1 schematically demonstrates the terminology commonly used to refer to an IRE pulse waveform. The polarity of a waveform (e.g., monopolar or bipolar) refers to whether its amplitude varies only in the positive direction or both in the positive and negative directions. The pulse width refers to the total "on-time," or time where the pulse is nonzero, and may be used to describe portions of the waveform in either the positive or negative direction, or both, depending on the context. The intra-pulse delay describes how much time passes before the completion of one pulse and the beginning of another, though it typically is used to describe the delay between pulses of opposite polarity in bipolar pulses. IRE treatment generally involves delivering tens to hundreds of pulses with a set amount of time between each pulse treatment repetition, and the inter-pulse delay is the amount of time between each pulse. The amplitude describes the magnitude of the potential in
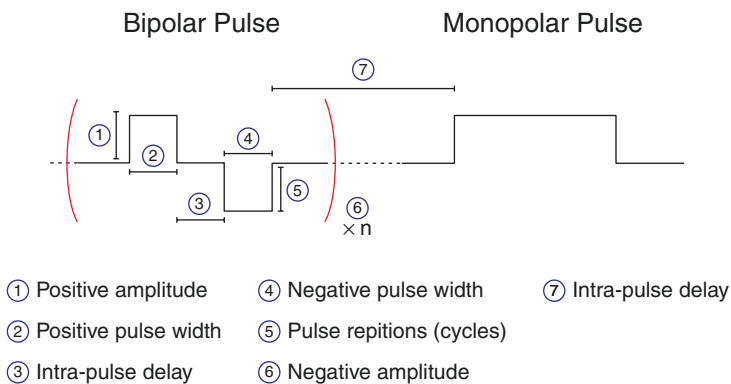

Fig. 3.1 Anatomy of bipolar and monopolar square electrical pulses. Waveforms commonly used in IRE are shown schematically to indicate terminology. A train of *n* bipolar pulses are shown followed by a single monopolar pulse

a single direction, measured from the sink electrode. These parameters may vary from treatment to treatment, but typically 80 pulses with pulse widths of 100 μs and repeated at once per second 1 Hz are used for an IRE treatment.

3.2.2   Ohm's Law

The relationship between an electrical potential V and the flow of electrical current I is frequently described as $V = IR$ where R is the degree to which a given material will resist the flow of current (resistance), which is the one-dimensional form of Ohm's law. Indeed, Ohm's law must be generalized to accurately represent geometries when considering complex tissue shape factors encountered when applying Ohm's law in more than one dimension. In multiple dimensions, the electrical field E arises from a potential drop between two points connected by path $\mathbf{l}$. The potential drop across that path provides the electric field along the orientation of $\mathbf{l}$ for every point along the path on each electrode and through tissue as

$$\Delta V = -\int_{x_1}^{x_2} \mathbf{E} \cdot d\mathbf{l}. \tag{3.1}$$

The electrical current is defined as the density of electrons flowing through a closed surface. Similar to the flow of a fluid driven by a pressure head, the flow of electrons is driven by a potential difference. In the fluid analogy, the total pressure head is equal to the integral of the pressure gradient at each point in the fluid flow. Similarly, electrical current flow is described by Eq. 3.1 in much the same manner: the total potential drop across a material is given by the electric field at every point integrated between the beginning and ending points.

Further extending the idea of electrical current using the fluid analogy, if we define the electrical current through a unit of volume, similar to a control volume in fluid dynamics, we obtain a current density $\mathbf{J}$. If $\mathbf{J}$ is defined at every point in a fluid flow, and we integrate across the entire fluid volume Ω (Fig. 3.2a), we can obtain a flow density $\mathbf{J}$ that gives the density of fluid (or electrons) and in which direction it is flowing. In order to measure such a density, we must define a surface in two-dimensional space through which $\mathbf{J}$ is flowing (Fig. 3.2b). For a simple fluid flow, this surface might be the cross section of a pipe. Abstracting this to an arbitrary unit surface\partial $d\Omega$, the flux integral

$$I = \oint_{\Omega} \mathbf{J} \cdot d\Omega \tag{3.2}$$

gives the current I as the integral of the current flow density $\mathbf{J}$ through an arbitrary closed surface\partial Ω. For a one-dimensional electron flow through a known cross section, Ohm's law is given as $V = IR$. However, visualizing two- and three-dimensional current paths and electric field distributions between two surfaces is slightly more complicated because the current does not travel homogeneously through the material but rather as a distribution such that the current density is spread throughout the entire ohmic material. Thus, the electrical current can be broken into its
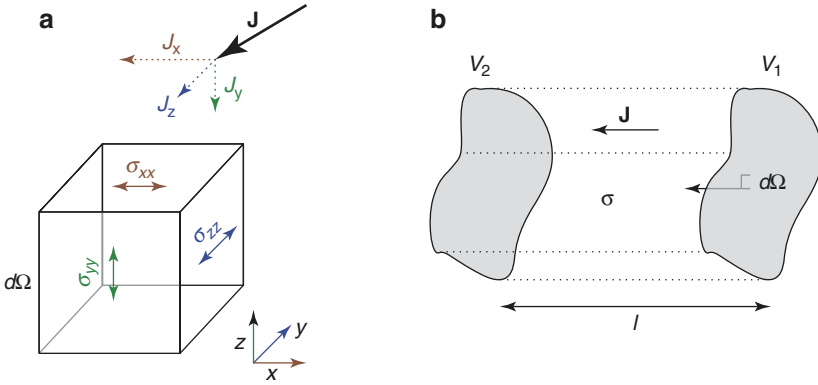
Fig. 3.2 Phenomenological relationship between electrical conductivity σ_{ij} and electrical current density $\mathbf{J} = <J_x, J_y, J_z>$. (**a**) Each component of the total electric current density vector $\mathbf{J}$ may experience a different conductivity through each unit component $d\Omega$ within an ohmic material. (**b**) A potential drop $\Delta V = V_1 - V_2$ between conducting surfaces separated by an ohmic material with conductivity σ results in a current density $\mathbf{J}$ through that material and an electric field of uniform intensity $|\mathbf{E}| = \Delta V/l$

vector components $\mathbf{J} = <J_x, J_y, J_z>$ where J_x, J_y, and J_z are magnitudes of electrical current density flowing in each the **x**, **y**, and **z** directions.

3.2.2.1 Electrical Conductivity

For an arbitrary geometry in the domain Ω, exposed to electric field $\mathbf{E}$, a current density $\mathbf{J}$ will develop in each of the x, y, and z directions. Thus, $\mathbf{J}$, described as the flow of electrons (electrical current) or ions (ionic current) per unit volume, is motivated by the electric field distribution within a given material Ω. For low-frequency or DC electric fields, we can relate $\mathbf{E}$ to $\mathbf{J}$ through Ohm's law on Ω as

$$\mathbf{J} = \underline{\sigma}\mathbf{E}. \tag{3.3}$$

where

$$\mathbf{E} = \begin{bmatrix} E_x \\ E_y \\ E_z \end{bmatrix}, \underline{\sigma} = \begin{bmatrix} \sigma_{xx} & \sigma_{xy} & \sigma_{xz} \\ \sigma_{yx} & \sigma_{yy} & \sigma_{yz} \\ \sigma_{zx} & \sigma_{zy} & \sigma_{zz} \end{bmatrix}, \mathbf{J} = \begin{bmatrix} J_x \\ J_y \\ J_z \end{bmatrix}.$$

Because the electrical potential drop as well as the current flow can occur in each spatial dimension, the conductivity $\underline{\sigma}$ must be represented as a 3×3 matrix (also called the conductivity tensor) that describes how the electric field in each direction can impact the current flows, or is conducted, in each dimension. For current flowing as the result of a potential drop within an arbitrary material in Cartesian coordinates, we can write

$$\begin{bmatrix} J_x \\ J_y \\ J_z \end{bmatrix} = \begin{bmatrix} \sigma_{xx} & \sigma_{xy} & \sigma_{xz} \\ \sigma_{yx} & \sigma_{yy} & \sigma_{yz} \\ \sigma_{zx} & \sigma_{zy} & \sigma_{zz} \end{bmatrix} \begin{bmatrix} E_x \\ E_y \\ E_z \end{bmatrix},$$

to show these interactions explicitly, where the subscripts on E and J indicate the direction of that vector component (i.e., J_x is the current density in the x direction) and the subscripts on σ are the ratio of each electric field component to each current density component (i.e., σ_{xy} is the ratio of the electric field component E_x divided by the current density component J_y). For a typical material, $\underline{\sigma}$ is generally symmetrical, meaning that

$$\underline{\sigma} = \begin{bmatrix} \sigma_{xx} & \sigma_{xy} & \sigma_{xz} \\ \sigma_{yx} & \sigma_{yy} & \sigma_{yz} \\ \sigma_{zx} & \sigma_{zy} & \sigma_{zz} \end{bmatrix} = \begin{bmatrix} \sigma_{xx} & 0 & 0 \\ 0 & \sigma_{yy} & 0 \\ 0 & 0 & \sigma_{zz} \end{bmatrix}. \tag{3.4}$$

3.2.2.2 Permittivity

Rather than simply allowing electron flow, a material may become polarized in the presence of an electric field at high frequencies. This behavior is known as permittivity. A material's permittivity describes its ability to become polarized in an electric field. This effect is due to the realignment of molecular dipoles motivated by the applied electric field. Permittivity is generally expressed relative to the permittivity of free space ϵ_0. Because it takes time for molecules to rearrange when the electric field is applied and removed (Fig. 3.3), the permittivity of a material gives rise to the transient response and may be thought of as the ability of a material to store electrical energy. Such properties are ideal in electrical components such as capacitors that are designed for this purpose. The capacitive current $\mathbf{J}_c$ through a material in a domain Ω with relative permittivity $\underline{\epsilon_r}$ is given as

$$\mathbf{J}_c = \epsilon_0 \underline{\epsilon_r} \frac{\partial \mathbf{E}}{\partial t}. \tag{3.5}$$

Similar to conductivity, $\underline{\epsilon_r}$ is given by the permittivity tensor
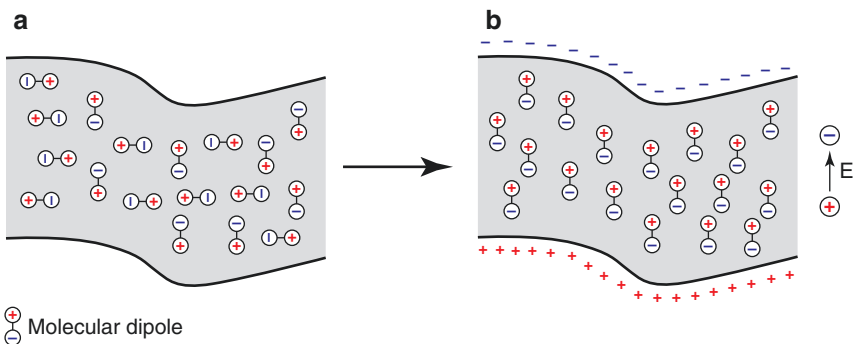

Fig. 3.3 Permittivity describes the extent to which a dielectric material composed of molecular dipoles or polarizable molecules to reorganize exposed to an electric field. The dipoles that are normally randomly distributed in a material (**a**) will realign with respect to the electric field **E** within a material (**b**). This results in the production of a capacitive current $\mathbf{J}_c$
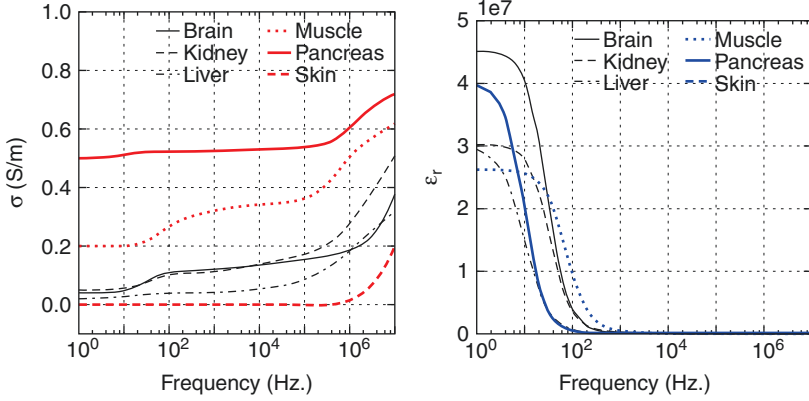
Fig. 3.4 Conductivity and relative permittivity of common tissues treated using electroporation-based therapies. The electrical conductivity σ (*left*) and relative permittivity ϵ_r (*right*) of common tissues are plotted for frequencies from 1 Hz to 1 MHz [17]

$$\underline{\epsilon}_r = \begin{bmatrix} \epsilon_{xx} & \epsilon_{xy} & \epsilon_{xz} \\ \epsilon_{yx} & \epsilon_{yy} & \epsilon_{yz} \\ \epsilon_{zx} & \epsilon_{zy} & \epsilon_{zz} \end{bmatrix},$$ (3.6)

which indicates how the capacitive current in each direction is generated through how the electric field changes in each direction over time. A material that exhibits such polarization properties is called a dielectric, and its relative permittivity ϵ_r may also be referred to as its dielectric constant. Oftentimes, a material can be considered isotropic, or possessing uniform material properties in every direction. Even if a material is not entirely isotropic on a molecular level, it may be considered such if the bulk conductivity, permittivity, and permeability are presented on a scale at which the material appears macroscopically homogeneous, such as in liver. In such cases, the tissue conductivity and permittivity can be determined generally throughout as a function of frequency, as depicted in Fig. 3.4. Introducing the capacitive current's dependence on angular frequency $\omega = 2\pi f$ (where f is given in Hz.) in a uniform material as $\mathbf{J}_c = \epsilon_r \epsilon_0 \omega \mathbf{E}$, we can write an equation stating that no current is generated within any point within the bulk of the material. This is known as the current continuity condition and can be written as [36]

$$(\sigma + j\epsilon_r \epsilon_0 \omega)\nabla \cdot \mathbf{E} = 0,$$ (3.7)

where $j = \sqrt{-1}$ is an imaginary number. By solving for $\mathbf{E}$, we obtain a modified expression similar to Ohm's law that accounts for the time-dependent changes present when the signal changes in time. This transient quantity, analogous to a tissue's ohmic resistance, is known as the tissue's impedance Z. However, in the course of integration, several spatial dependencies must be considered, though, if conductivity and permittivity are constant in space and time, the spatial component of the material's impedance may be represented by the shape function K. In this case, the impedance of a tissue is given as

$$Z = \frac{1}{K\left(\sigma + j\epsilon_r \epsilon_0 \omega\right)}. \tag{3.8}$$

Shape functions will be discussed further in the following section, though the transient response of a material may be estimated using Eq. 3.8 to estimate the impedance of a material with uniform, static conductivity and permittivity. Because biological tissue's properties change relatively slowly compared to the duration of the applied electric field in a typical IRE procedure, the electrical properties are considered quasi-static and are estimated at low frequencies (DC-1 kHz).

3.2.2.3 Shape Functions

For a material with no transient response in more than one dimension, we adapt Ohm's law to multiple dimensions using a shape factor K such that the total resistance of the material R is given by
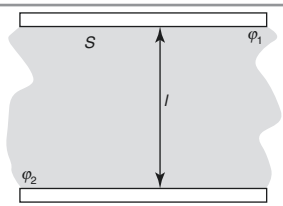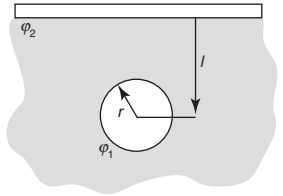
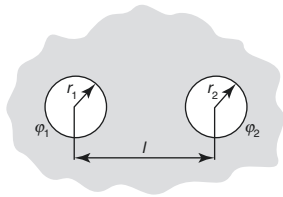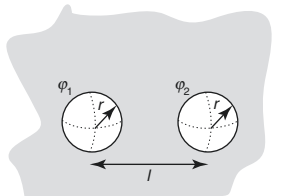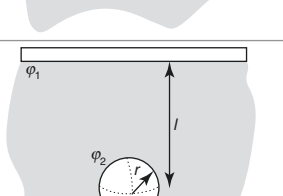$$R = \frac{1}{K\sigma}. \tag{3.9}$$

Representing Ohm's law in this manner greatly simplifies the estimation of tissue properties from the electric field distribution using readily measurable quantities, voltage V and current I. Shape factors calculated for several common electrode geometries in an electrically homogenous material are given in Table 3.1. For example, in the case of an ohmic material separated by two large conducting plates, the shape factor given in Table 3.1 is $K = A/l$, where A is the surface area of the plates and l is the distance between them. In this case, the resistance of the material is given as $R = l/(A\sigma)$, which corresponds to the general resistance of a short cylinder.

This example illustrates two particularly useful concepts in developing an intuition with regard to how electric fields behave. If the area of the electrodes in this geometry is increased, the total effective resistance of the system is decreased, meaning that more total current will flow through the material. However, the current going through the system may be decreased if the distance separating the two plates is increased. These relationships are intuitively true in a given geometry, and their interplay is helpful in understanding a material's response in the presence of an electric field.

3.2.3 Laplace's Equation

Given a homogenous material exposed to an electric field, the conductivity (and permittivity, in the case of a dielectric) may be divided from both the right- and left-hand sides of the continuity equation, leaving $\nabla \cdot \mathbf{E} = 0$. Considering the definition of an electric field $\mathbf{E} = -\nabla \varphi$, the general form of an electrostatic field can be solved by Laplace's equation as

Table 3.1 Shape functions for calculating the electrical resistance in a tissue for a given electrode configuration

Electrode geometry		Shape factor (K)
Parallel plates of surface area A separated by a material of length l		$\dfrac{A}{l}$
Cylinder and plate for which $d \gg r$ and $A \gg r$, d and d is the cylinder length		$\dfrac{2\pi d}{\cosh^{-1}(l/r)}$
Parallel cylinders of length d in an infinite material for which $l \gg r_1, r_2$		$\dfrac{2\pi l}{\cosh^{-1}\left(\dfrac{2l^2 - 2r_1^2 - 2r_2^2}{r_1 r_2}\right)}$
Two spheres in an infinite material and for which $r_2 \geq r_1$		$\dfrac{4\pi r_2}{\dfrac{r_2}{r_1}\left(1 - \dfrac{(r_1/l)^4}{1-(r_2/l)^4}\right) - \dfrac{2r_2}{l}}$
Sphere and plate in a semi-infinite material and for which $l > r$		$\dfrac{4\pi r}{1 - r/(2l)}$

Adapted from Bergman et al. [4]
To calculate resistance, use $R = 1/(\sigma K)$ where K is the shape function listed in the right column

$$\nabla^2 \varphi = 0 \qquad (3.10)$$

where φ is the local electric potential field and the Laplacian operator is defined for Cartesian coordinates as $\nabla^2 \varphi = \varphi_{xx} + \varphi_{yy} + \varphi_{zz}$. From a physical perspective, Laplace's equation indicates that no electric field source exists within the material

Table 3.2 Typical electrical properties of cellular components of an isolated cell

Parameter	Variable	Value	Unit	Reference
Permittivity of free space	ϵ_0	8.854×10^{-12}	*As/Vm*	
Extracellular (saline) relative permittivity	ϵ_e	75		[6]
Extracellular (saline) conductivity	σ_e	1.25	*S/m*	Measured
Cell membrane relative permittivity	ϵ_m	7		[22]
Cell membrane conductivity	σ_m	3×10^{-7}	*S/m*	[19]
Cell membrane thickness	d_m	4	*nm*	[3]
Cytoplasm relative permittivity	ϵ_i	60		[21]
Cytoplasm conductivity	σ_i	0.5	*S/m*	[22]
Cell radius	r	10	μm	

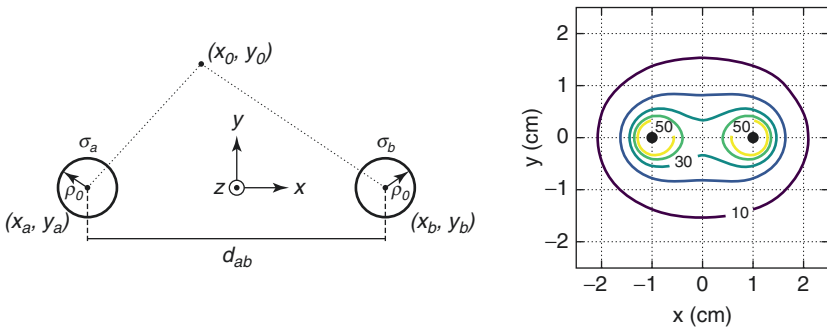Adapted from Čemažar et al. [8]

Fig. 3.5 The solution to Laplace's equation for two infinitely long cylindrical electrodes. The solution to Laplace's equation is given for the case of 1.0 V applied across 0.1 cm (ID) cylindrical electrodes spaced 2.0 cm apart. Contours are given for 10, 20, 30, 40, and 50 V/cm (Adapted from Mahnic-Kalamiza et al. [28])

and can only exist at the boundaries. From here, modeling the electric field distribution for a particular geometry is performed by solving Laplace's equation in each subdomain with a given material property using the isopotential and current continuity boundary conditions giving an electric field distribution. For the case of two cylindrical electrodes, the solution to Laplace's equation is shown in Fig. 3.5.

3.2.3.1 Parallel Plate Electrodes

The simplest geometry for which an electric field may be calculated is that of two conductive parallel plates of surface area A separated by distance d (with the condition that $A \gg d$). The electric field intensity within the material may then be approximated along a single dimension as $\mathbf{E} = -\nabla\varphi \approx -\Delta V/d$. By scaling the total current I for a unit surface area on the conducting electrode as I/A, Ohm's law confirms the shape factor given in Table 3.1, yielding

$$\Delta V = RI = \frac{l}{A\sigma}I,$$

after rearrangement. It is important to note that though the electric field is equivalent to the voltage-to-distance ratio in the case of parallel plate electrodes, this is not always the case, and the reader should exercise prudence when applying the principles herein described for more complex geometries.

3.2.3.2 Two Cylindrical Electrodes

Electrode configurations consisting of two or more cylindrical, needle electrodes are almost ubiquitously used in ECT, GET, and IRE. An analytical solution exists for the electric field intensity as a function of position around the electrode insertions in the plane perpendicular to the exposed conductors. The electric field due to two long, cylindrical electrodes of equal radius $r_a = r_b = \rho_0$ placed at positions (x_a, y_a) and (x_b, y_b) with their centers offset by distance d_{ab} is given as

$$E(x_0, y_0) = \frac{\varphi_{ab}}{2\log\dfrac{d_{ab} + \sqrt{d_{ab}^2 - 4\rho_0}}{2\rho_0}} \cdot$$

$$\sqrt{\left(\frac{x_a' - x}{\left(x_a' - x\right)^2 + \left(y_a' - y\right)^2} - \frac{x_b' - x}{\left(x_b' - x\right)^2 + \left(y_b' - y\right)^2}\right)}$$

$$\sqrt{+\left(\frac{y_a' - y}{\left(x_a' - x\right)^2 + \left(y_a' - y\right)^2} - \frac{y_b' - y}{\left(x_b' - x\right)^2 + \left(y_b' - y\right)^2}\right)^2} \tag{3.11}$$

for the general form of the analytical solution for two electrodes [9, 28] to Eq. 3.10, with constants as

$$x_a' = x_a + |e| \cdot \sin\theta_1, \theta_1 = \arctan\frac{y_b - y_a}{x_b - x_a},$$

$$x_b' = x_b + |e| \cdot \sin\theta_2, \theta_2 = \arctan\frac{y_a - y_b}{x_a - x_b},$$

$$y_a' = y_a + |e| \cdot \sin\theta_1,$$

$$y_b' = y_b + |e| \cdot \sin\theta_2, e = \frac{d}{2} - \sqrt{\left(\frac{d}{2}\right)^2 - \rho_0^2}.$$

From this calculation, several particularly important phenomena arise that may not be obvious. From inspection of Eq. 3.11, we recognize that the electric field does not decay linearly between the two electrodes—i.e., the voltage-to-distance ratio does not provide a valid representation of the local electric field intensity,

dramatically overestimating the treatment result. The electric field intensity distribution for this geometry is plotted in Fig. 3.5, and it quickly becomes clear that the shape of the electric field in this configuration appears to resemble the two-dimensional projection of a peanut or an infinity symbol: the electric field intensity is greatest near the electrode and decays radially between them. Consequently, any electric field-dependent phenomenon will occur first at the electrode-tissue interface first before propagating throughout the remaining exposed tissue.

The two-needle electrode geometry may be extrapolated to an arbitrary number of electrodes placed around a target tissue volume. For N electrodes positioned around a tissue mass, the electric field distribution is given by the superposition of the electric fields generated by each electrode, depending on the geometry and the sequence in which the electric field is applied [14] (Fig. 3.12). However, there are several important consequences of arranging electrodes in arrays and then energizing pairs of them in sequence. By energizing any pair electrodes following a different pair, the total electric field experienced within the total tissue is a sum of the electric fields generated by each of the electrode pairs. While this may not significantly impact the electric field distribution in a tissue with static conductivity and permittivity, the electrical properties of biological tissue change as a function of electric field intensity, temperature, and time. In a realistic procedure, the electric field distribution between any two sets of electrodes in an array will be dependent on the electric field distribution generated between the previously energized electrode pairs. This will effectively manifest as unequal resistances measured between two otherwise geometrically similar electrode pairs. Though IRE schemes are designed to largely account for these differences, they will nevertheless be present, and similar resistance measurements should not be expected.

3.3   Cell-Level Phenomena

In general, biological tissue has a very hierarchical structure; a tissue's smaller scale components dictate its gross anatomical form. Specifically, in the case of electroporation-based treatments and therapies, the biophysical action of the treatment at a molecular level dictates the cellular effects which, in turn, dictate the tissue and organ-level outcome of the treatment. It is because of this structure that attaining a holistic understanding of electroporation processes at the cellular level helps caregivers exploit the relevant physical mechanisms to attain more accurate and clinically advantageous treatment plans and protocols.

3.3.1   Transmembrane Potential and the Schwan Equation

The cellular membrane functionally separates the interior of a cell from its external environment, thereby establishing chemical gradients that the cell utilizes for generating action potentials, nutrient uptake, and waste export. These chemical gradients establish an osmotic gradient across the relatively impermeant membrane. Due to the electrical charge distribution within many of these molecules, the chemical gradient established across the cell membrane also establishes a large electric

potential difference (~70 mV). When an electric field is applied across a cell, opposing charges gather at opposing sides of the membrane and generate an electrically induced pressure across the membrane. When this pressure surpasses a threshold, defects in the membrane are expanded and allow molecular transport into and out of the cell. This is the mechanistic basis for electroporation.

In 1957, H. P. Schwan developed the expression now carrying his name for the transmembrane potential induced by an exogenous electric field applied to a spherical cell [41]. The Schwan equation is commonly employed to provide an intuitive, analytical description of the mechanism giving rise to electroporation phenomenon. The formulation of the Schwan equation considers concentric spherical regions to represent a cell. The transmembrane potential is the difference in potential in the radial direction across the thin region separating the center region of the concentric spheres defining the membrane boundaries; in other words, the membrane is modeled as the dielectric shell. In such a case, the transmembrane potential is defined as

$$\varphi_m(r,\theta) = f_s ER\cos(\theta),\tag{3.12}$$

where

$$f_s = \frac{2\sigma_e\left[3d_m R^2\sigma_i + \left(3d_m^2 R - d_m^3\right)\left(\sigma_m - \sigma_i\right)\right]}{2R^3\left(\sigma_m + 2\sigma_i\right)\left(\sigma_m + \frac{1}{2}\sigma_i\right) - 2\left(R - d_m\right)^3\left(\sigma_e - \sigma_m\right)\left(\sigma_i - \sigma_m\right)}.$$

In this case, the cell membrane has a thickness of d_m, and the radius of the cell to the internal surface of the membrane is R. The conductivity of the cytoplasm, membrane, and extracellular medium are given as σ_i, σ_m, and σ_e, respectively. In reality, there is a time dependence on the induced transmembrane potential φ_m. This time dependence can be approximated through further simplifications performed under the conditions that the membrane diameter is much smaller than the radius of the cell ($d_m << R$). Through substitution of $\sigma + j\epsilon_r\epsilon_0\omega$ for σ in order to obtain the transient components of the transmembrane potential given by the Schwan equation and if the permittivities of the internal and the external electrolytic media are negligible ($\epsilon_i \approx \epsilon_e \approx 0$), and the conductivities of the internal and external media are significantly greater than that of the membrane ($\sigma_m << \sigma_i,\sigma_e$), the membrane charging time constant τ is given by

$$\tau = \frac{R\epsilon_m}{2d_m\left(\dfrac{\sigma_i\sigma_e}{\sigma_i + 2\sigma_e}\right) + R\sigma_m}.$$

We may now rewrite the time-dependent Schwan equation as

$$\varphi_m(r,\theta,t) = f_s Er\cos(\theta)\left(1 - \exp\left(-\frac{t}{\tau}\right)\right),\tag{3.13}$$

which demonstrates how the transmembrane potential depends on the geometric contributions of the cell shape f_s, the exponential dependence on time t, and the polar
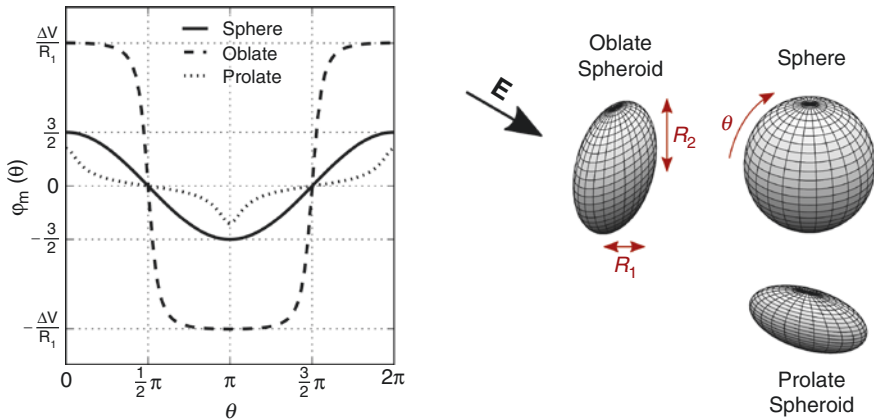
Fig. 3.6 The surface area of the cell membrane experiencing a significantly increased transmembrane potential $\varphi_m(\theta)$ is increased for cell geometries perpendicular to the electric field. The transmembrane potentials induced on spherical and oblate and prolate spheroidal cells are plotted and indicate that the greater the projection of the cell surface parallel to the electric field, the greater the area on the cell membrane that experiences significantly increase transmembrane potentials (Adapted from Kotnik and Miklavcic [26])

position θ. We must consider that cell geometry and orientation with respect to the electric field affect the induced transmembrane potential. The transmembrane potentials resulting from extending our analysis to prolate and oblate spheroidal geometries with interior membranes (shells) are shown in Fig. 3.6 [25, 26]. The transmembrane potential profiles shown in Fig. 3.6 highlight how the regions of the cell surface perpendicular to the electric field experience the greatest transmembrane potential, resulting in the greatest probability of electroporation in these areas. It is important to note that the transmembrane potential expression is similar for prolate, oblate, and spherical cells; the oblate geometry experiences a considerably larger surface area of the membrane to larger transmembrane potentials than the prolate geometry. In practical terms, this indicates that cells positioned with their long axes perpendicular to the electric field (oblate) will exhibit a significantly greater average membrane permeabilization than if their long axis is parallel to the electric field.

3.3.2 Pore Generation in Bilayer Lipid Membranes

In 1979, Abidor et al. were able to link the increased conductivity and molecular transport observed post-exposure in bilayer membranes to membrane defects arising from the colloidal nature of lipid bilayers [1], and in so doing, developed the biophysical explanation underpinning modern electroporation theory.

An intact bilayer membrane will form spontaneously in an aqueous material. Once formed, a membrane is subject to thermodynamic fluctuations that govern its structural properties at the molecular level; the distance between charged lipid head groups fluctuates while maintaining the hydrophobic membrane core because of the random thermodynamic motion of the lipid molecules [24]. Representing these
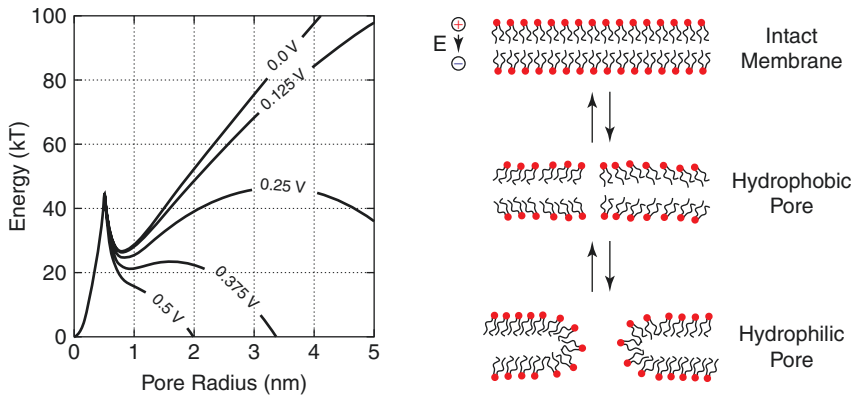
Fig. 3.7 Energy of pore formation becomes favorable with increasing transmembrane potential. A membrane defect that forms as a result of normal thermal fluctuations of the cell membrane increase in radius is forced to expand in the presence of an increased transmembrane potential—a hydrophilic pore—and eventually cause the lipid head groups to invert when the defect has reached a critical radius $r = r_*$ to energetically stabilize the structure, forming a hydrophobic pore

random fluctuations as a statistical distribution, it becomes conceivable that there is a small probability that the random motion of the lipid molecules in the bilayer membrane will generate a defect in the membrane structure in which an intramolecular space will form that is large enough to permit a molecule to penetrate the hydrophobic core and emerge on the opposite side (Fig. 3.7). Though not explicitly detailed here, the derivation of the following interfacial physics calculation is detailed in [1, 20, 29, 30] for interested readers. In 1999, DeBruin et al. simplified the explanation of the second type of defects that form as hydrophilic pores by introducing a quadratic term to represent the energy of this enlarged defect—termed a hydrophobic pore—rather than the modified Bessel functions used previously [13] (Fig. 3.7).

Once the radius of a defect reaches a critical value, denoted $r = r^*$, the lipid head groups invert and energetically stabilize the pore, bridging the two membrane leaflets and creating a hydrophilic pore. This stabilization is reflected as a local minimum in the energy function $r_m > r^*$ and indicates that, once hydrophilic pores are formed, they tend to aggregate at $r = r_m$ before collapsing back to an intact membrane. Physically, these dynamics are captured by modeling a hydrophobic pore using the quadratic term proposed by DeBruin et al. such that a global minimum energy is achieved at $r = 0$, where the hydrophobic pore of radius is normalized to the radius at which the hydrophilic-hydrophobic transition occurs r^*. The energy associated with that transition is denoted as $E(r_*) = E_*$. The hydrophilic pore energy is developed by considering a dielectric material separating two bulk phases of a conducting material. The term $\pi a_p r^2 \varphi_m^2$ represents the electrical energy that motivates the transition of a hydrophobic to hydrophilic pore, similar to a discrete capacitor. The inside of a hydrophilic pore is associated with a linear tension $2\pi r\gamma$, and whole membrane experiences a surface tension $\pi r^2 \Gamma$. An additional term is added here as a quartic term to represent the steric interactions of the lipid head groups in

the pore with C as the interaction constant. Together, with the introduction of an exogenous electric field added to the energy function

$$E_{pore}(r) = \begin{cases} E_*\left(\dfrac{r}{r_*}\right)^2 - \pi a_p r^2 \varphi_m^2 & 0 \le r \le r_* \\ \\ 2\pi r\gamma - \pi r^2\Gamma - \pi a_p r^2 \varphi_m^2 + \left(\dfrac{C}{r}\right)^4 & r_* < r \ll d_m \end{cases}, \quad (3.14)$$

where φ_m is the transmembrane potential and a_p accounts for the difference in dielectric properties between an intact membrane and the surrounding aqueous environment, estimated as [1, 38]

$$a_p = \frac{(\epsilon_w - \epsilon_l)\epsilon_0}{2d_m}.$$

Figure 3.7 shows the altered pore energy function arising from increased transmembrane potentials. It is of note that dramatic deformation for $r > r_*$ occurs at potentials ~200 mV and has been estimated experimentally to be between 0.2 and 1 V [39].

3.4   Electric Field Distribution in Gross Tissue

Through our discussion of the effects of an electric field on a single cell, we can expand the discussion to multicellular and tissue-level systems. With the understanding that the electric field intensity, frequency, and waveform are the most easily manipulated parameters to adjust for electrode arrays of a fixed geometry, and that the transmembrane potential both directly depends on the magnitude of the applied electric field and drives electropore formation, a tissue-level perspective of the effect of electric fields in vitro may be quickly developed. With the electric field intensity driving electroporative processes, such as IRE, it becomes critical to predict the electric field distribution within a biological tissue. At frequencies <10 kHz, it is commonly assumed that the electric field distribution may be approximated using the Laplace equation. In this case, the tissue is only considered resistive, with no capacitive component. While this assumption provides an incomplete model for tissue, it is nonetheless widely used and provides valuable information. The typical frequency content of an electrical signal used in clinical applications of electroporation is below 10 kHz, and, as such, our discussion will focus on the tissue response within this range.

3.4.1   Deviations in Electrode Geometry

Idealized plate electrodes are considered completely planar, while cylindrical electrodes are considered perfectly cylindrical and parallel. However, in reality,

scenarios present where it becomes necessary to account for slight variations in intraoperative electrode placement and positioning. For example, electrodes may be placed slightly skew, or a particularly dense tissue region may cause electrode bowing or off-parallel insertion when using needle electrodes. Though these variations may appear slight, they may result in suboptimal, incomplete, or excessive ablation.

3.4.1.1 Bowing and Angulation

Inserting and maintaining parallel two-needle electrodes into a highly structured tissue, even with guides and sharpened ends, may prove challenging due to multiple tissue layers, dense connective tissue, or soft tissue deformation during treatment. This angulation results in an intensification of the electric field and current density toward the conducting surfaces in closest proximity Fig. 3.8. Significant angulation may result in the incomplete ablation of tissue regions where the conducting surfaces of the electrodes are farthest apart and, though complete ablation occurs around the surfaces of electrodes in close proximity, unwanted heat may be generated in this region due to the increased current density driving increased Joule heating (discussed later). Though addressed individually, these aberrations may be
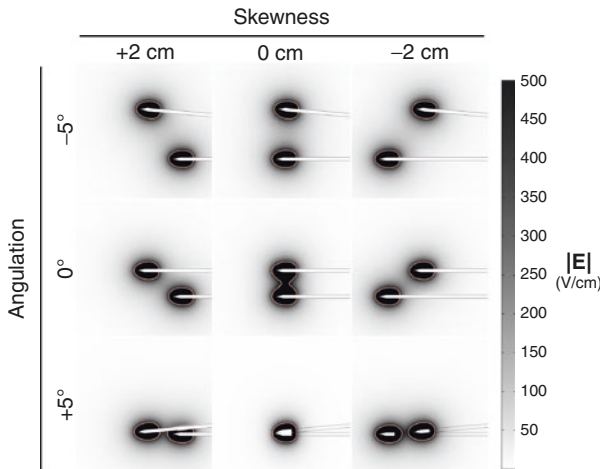

Fig. 3.8 Angulation and skewness of exposed electrode surfaces can significantly impact the electric field intensities driving electroporation within the target tissue region. In simulated, isotropic liver tissue ($\sigma = 0.1$ S/m, $\epsilon_r = 80$), cylindrical needle electrodes with radii of 1 mm and sharp conical tips are inserted 10 cm into the simulated tissue mass. One centimeter of the conducting surface of the electrodes, excluding the tip, was exposed on each electrode, and simulations are given at steady state, without considering dynamic conductivity tissue responses to the electric field or temperature. 1.5 kV were applied to the two electrodes, which are spaced 1 cm apart in the central image

compounded and result in over- and under-exposed tissue regions to be suboptimally or ineffectively treated.

When electrodes deform along their length during placement—called bowing—regions of tissue may experience increased or decreased electric field intensities because the electrodes are closer or further apart, respectively. Bowing, similar to angulation, may cause regions of underexposed tissue to remain insufficiently permeabilized to effectively enhance molecular transport or to induce cell death. Overexposed regions will experience increased Joule heating and may be more susceptible to unintended thermal damage.

3.4.1.2 Skewness

For an ideal placement, electrodes are often placed in the same plane and focally ablate the tissue region between the exposed conductors. However, scenarios present where electrodes may not be inserted to exactly the same depth because of sensitive tissue structures or other such anatomical consideration. In this case, it is imperative to consider the ratio of the characteristic length of the exposed conducting surface on the electrodes to the distance between them. If not properly handled, skew electrodes can either cause an underestimation of the tissue treatment volume because a greater distance than expected separates the two electrode surfaces. However, if well considered, a skewed electrode placement can confer the benefit of being able to more elegantly deliver the electric field intensities necessary for IRE to a tissue region with complexities such as vascularity or anisotropy.

Generally, though, for an isotropic tissue, angulation will result in an overestimate of the ablation volume because the physical distance separating the two electrodes will be greater. This greater distance may not matter for slightly skew configurations of a few millimeters but will significantly impact the treatment volume when the distance between electrode surfaces is more than about half of their height of the electrode. However, if the two electrodes are placed in close lateral proximity (i.e., the shaft of the two electrodes are close together) and separated by roughly the distance similar to that of the exposed electrode surface, the ablation volume will appear ellipsoidal along the axis of the electrode shafts.

In general, the ratio of conductor surface areas to the distance separating them indicates whether the electrodes generate an electric field with a conduction shape function that will more closely resemble a point source and a semi-infinite plane or a parallel electrode configuration. Small differences in exposed surface area will not significantly impact the electric field, so long as the electrodes are approximately symmetric around a central axis. It is important to recognize the distortions that may be present under these circumstances.

3.4.1.3 Tissue Inhomogeneity

Tissue structure and orientation are complicated by the presence of multiple tissues performing multiple tasks in close proximity; a tissue's electrical properties are derived from this structural organization. Therefore, a tissue's physiology must be carefully considered in pretreatment planning for IRE procedures.
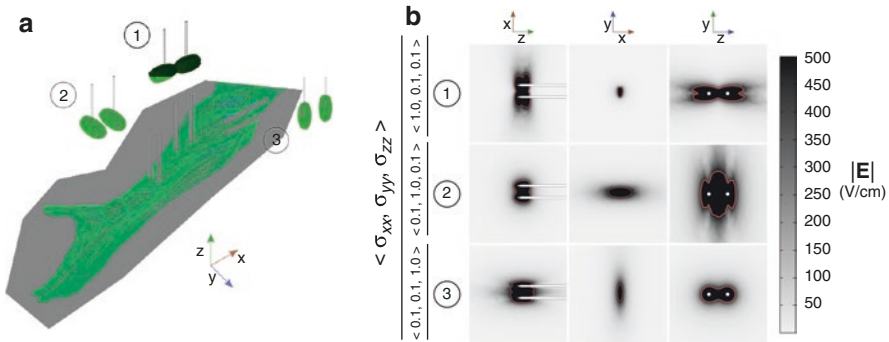
Fig. 3.9 A tissue exhibiting anisotropic conductivity will distort the expected electric field depending on the electrode placement. Electrodes were inserted into simulated anisotropic tissue (muscle; $\epsilon_r = 80$; $\underline{\sigma} = \left\langle \sigma_{xx}, \sigma_{yy}, \sigma_{zz} \right\rangle$) at the points shown in (**a**), and the lesion geometries around the electrodes are indicated by the surfaces around the electrode tips. The electric field distortions generated in the *xy*-, *yz*-, and *xz*-planes as a result of different anisotropic conductivities are shown in (**b**). The electric field was generated using an applied potential of 1.5 kV, and the 500 V/cm electromagnetic intensity isosurface of the resultant electromagnetic field distribution is shown. The axis indicator refers to the electrode positioning of the images with the electric field isosurfaces rather than the orientation in (**a**); this orientation is conserved in (**b**)

3.4.1.4 Anisotropic Tissue

Electrical anisotropies arise from asymmetric distributions and orientations of tissue and its constituents that allow electrical current to flow in one direction more easily than another Fig. 3.9. Physically, these anisotropies mean that the conductivity tensor σ_{ij} is not equal in each coordinate direction ($\sigma_{xx} \neq \sigma_{yy} \neq \sigma_{zz}$) and that the electric field distribution will be distorted because the electron flow will be directed according to the particular anisotropy. For example, muscle tissue is highly anisotropic as the muscle fibers stretch along the contractile axis of the tissue. This structure allows electrical current to flow more easily along the contractile axis with the fiber alignment, rather than against it.

3.4.1.5 Vascularization and Perfused Tissue

During exposure to electric fields, fluid flow and the vascular structure itself generate inhomogeneities within the tissue that complicate the prediction of its response Fig. 3.10. If the perfusate is an electrolyte, for example, blood flowing through the portal vein in the liver, it may conduct electric current better than the surrounding tissue and result in a large anisotropy along the axis of fluid flow at the local vessel region. Conversely, the vascular walls produce a large capacitance that introduces a nontrivial time dependence into the electric field distribution that might not be present in relatively homogeneous bulk tissue, like the lobe of a liver.

3.4.2   Joule Heating

Thermal considerations are critical when planning and delivering IRE treatment to a target tissue region. While delivering electric current to a tissue, it may be
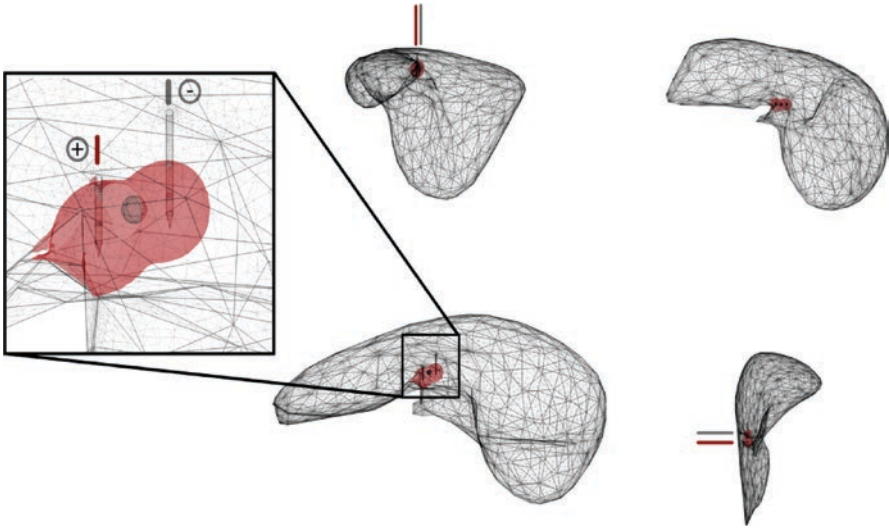
Fig. 3.10 The electric field surrounding tumor tissue embedded in normal vascularized tissue (liver) will distort the electric field delivered to the target tissue. A simulated liver tissue with static electrical properties (to emphasize the effect of inhomogeneous tissue) is shown with the gallbladder, hepatic ducts, liver lobule tissue, and falciform ligament each exhibiting different electrical properties. The electric field surface shown for a potential ablation zone is shown from the (**b**) right dorsal sagittal, (**c**) left dorsal sagittal, and (**d**) superior transverse perspectives. Distortions in the electric field occur at the tissue-tissue and tissue-air boundaries

important to deliver series of pulses, but it is critical to understand that thermal energy is generated when electrical current travels through a resistive material. When electrical energy is consumed by a material, the rate at which it is consumed is given by the rate of energy conversion (power $\wp$)

$$\wp = \mathbf{J} \cdot \mathbf{E} = \sigma \left| \mathbf{E} \right|^2 .$$

In the case of biological tissue undergoing IRE treatment, this energy delivered to the tissue is largely transformed into heat. It is desirable for the thermal damage sustained by a tissue to remain minimal so that protein denaturation does not occur and the structural integrity of the proteinaceous stromal components is not compromised [11, 18, 35].

For a particular point in space, the heat generated in a unit volume of tissue Q is given as $Q = \wp$, assuming perfect conversion from electrical energy to heat (i.e., $Q = \sigma|\mathbf{E}|^2$). Thus, the material conductivity σ directly impacts the heating of the tissue as a result of the electrical energy. Generally, the temperature distribution and the change in temperature for a region of tissue undergoing IRE treatment are calculated by Pennes bioheat Eq. 3.10 with an added term to account for Joule heating, which is given by

$$\rho c_p \frac{\partial T}{\partial t} = \nabla \left(\kappa \nabla T \right) + \dot{q}_m + \dot{q}_p + \sigma \left| \mathbf{E} \right|^2 \qquad (3.15)$$

where ρ is the density of the material, c_p is the heat capacity of the material, T is temperature, $\dot{q}_m$ is the heat generated from metabolic processes within the tissue, and $\dot{q}_p$ is the heat added to the tissue by a perfusate.
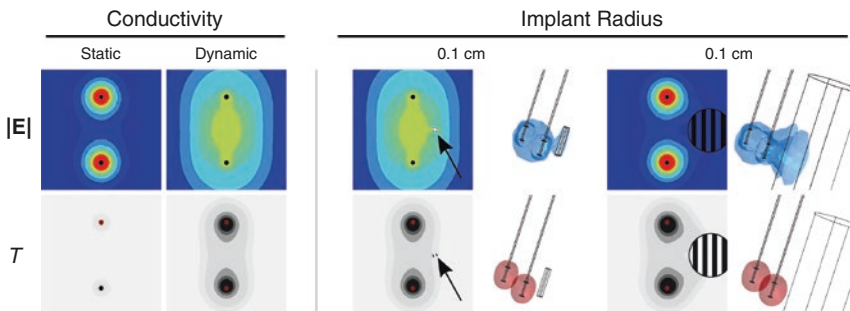
3.4.2.1 Dynamic Conductivity

The cell membrane serves as a barrier across which chemical and electrical potential gradients are established to drive cellular processes. When cells become electroporated, the membrane develops pores which permit the diffusive exchange of normally impermanent molecules between the intracellular and extracellular environment. This affects the electrical properties of a bulk tissue by both increasing the conductivity of the extracellular material [23, 37] from the cytoplasm and opening previously unavailable intracellular current pathways.

The bulk electrical conductivity of a tissue changes as a result of increased cellular permeability during application of electric fields to a target tissue from empirically determined local electric field intensity as a function of the local electric field intensity and temperature for a given point in space is given by

$$\sigma_D\left(E,T\right)=\left(1+\alpha(T-T_0)\right)\left[\sigma_0+\left(\sigma_{max}-\sigma_0\right)\exp\left(-A\exp\left(-B|\mathbf{E}|\right)\right)\right]$$

where T is the temperature, T_0 is the initial temperature, α is the conductivity-temperature coefficient ($\sim$ 1–3 %/°C) [34], σ_0 is the initial electrical conductivity, σ_{max} is the electrical conductivity obtained when the tissue is maximally permeabilized, E is the electric field intensity, and A and B are curve-fitting terms [34].

To illustrate the impact of intraoperative electrical conductivity changes arising from temperature changes and exposure to electric fields, a simulated liver tissue is shown in Fig. 3.11 to demonstrate the altered electric field and temperature

NOTE: The same values were used for the contours arcross all images

Fig. 3.11 Dynamic conductivity and large conductive obstructions dramatically distort the electric field distribution. Biological tissues increase their conductivity in applied electric fields as cells become electroporated. The electric field for the cases of static (σ) and dynamic conductivity $\sigma(|\mathbf{E}|,T)$ are *plotted* in the *right panel*. The *left* shows the distortions in electric field created by the presence of an electrically conductive object near the electrodes delivering IRE pulses with larger obstructions affecting the electric field distribution more than small obstructions. Temperature distributions are also given for each scenario and indicate that the temperature distribution is similar to the electric field distribution

distributions. It is important to note that the tissue was considered without perfusion and metabolic components to isolate the impact of the electric field, geometry, and temperature on the conductivity distribution throughout the tissue. The left panel shows a static homogenous conductivity ($\sigma = 0.15$ S/m) and a dynamic conductivity based on the dependence given by Sect. 4.2.1. While in the case of a static conductivity σ, the electric field distribution closely mirrors that predicted by Eq. 3.11; when a dynamic conductivity $\sigma(\mathbf{E}, T)$ is used, the electric field is distorted, and the electric field intensity becomes more evenly distributed across the tissue between the electrodes because the current flowing between the electrodes is able to be distributed across a larger, more conductive region. The increased conductivity of this region will necessarily permit more current under equipotential pulses and is responsible for the change in resistance measured between the first pulse and the last pulse in a train [15].

3.4.2.2 Pulse Number

IRE has typically been performed using a recommended 70–90×100 μs pulse delivered once every 1.0 s (1 Hz) at voltages that depend on the target tissue, desired ablation volume, and electrode geometry [2, 42]. This setting was chosen because it delivers the optimal number of pulses to achieve efficient cell death throughout the tissue volume while mitigating thermal damage resulting from Joule heating [10, 35]. Delivering more pulses will result in a growth of the ablation zone due to the conductivity changes in the tissue and the greater probability that cells within the ablation zone will be destroyed; though this could dramatically impact the thermal damage to the tissue. With increasing pulse number, the ablation zone size will initially make significant increases with pulse number during the first ~70–90 but only marginally impact its size for the following pulses. However, increasing pulse number, for equivalent-length pulses below the capacity of the tissue to diffuse the heat generated by a single pulse, also increases the heat generated in that tissue. Delivering a train of hundreds of pulses may not, effectually, impact the efficacy of IRE to kill cells but will certainly increase the heat generated within and around the electrodes and ablation region [35]. For this reason, it is critical to balance the pulse number with minimal thermal damage to the tissue.

Several strategies to minimize tissue heating during IRE procedures have previously been employed. Simply adding inter-pulse delays between each pulse allows some heat to diffuse away from the ablated tissue and results in less overall temperature rise. In a similar vein, performing a train of pulses in rapid succession followed by a longer delay achieves a similar effect, though with potentially larger ablations generated within each cycle. Actively cooling the ablation region using a heat sink would further mitigate IRE's thermal effects by actively drawing excess heat out of the tissue instead of allowing it to passively diffuse. Though the specific details of these methodologies are not outlined here, increasing pulse number also increases the concern for undesired thermal effects and spurs the need for effective cooling.

3.4.2.3 Conductive Implants

Metallic surgical implants (stents, bone screws, etc.) or instruments (other electrodes, hemostats, etc.) have become commonplace, and it must be understood that introducing such a material to an electrical environment will distort the electric field distribution at an extend proportional to its size and conductivity relative to the size and conductivity of the affected tissue. For example, small objects (treatment seeds) will have a trivial impact, whereas larger objects (stents) will have a greater effect. The conducting metallic surface will result in the buildup of surface charge which diverts the flow of electrons with respect to that obstruction. However, a conducting obstruction on the order of the same diameter as the needle electrodes does not significantly distort the final ablation volume, and it has been shown that such structures do not impede the safe and effective delivery of IRE treatment [33, 40]. Similarly, the temperature distribution in a tissue is relatively unchanged for small conductive obstructions, with larger obstructions impacting the temperature distribution more significantly, assuming they begin at the same temperature as the surrounding tissue. However, if these obstructions begin at cooler temperatures, they may serve as heat sinks for heat transfer and ultimately generate lower temperatures throughout the ablation region, if heating becomes a concern.

3.4.2.4 Electrode Exposure Length

The exposed length of the conductive electrode surface can also impact the electric field distribution in an ablation region. For example, if only a small portion of the electrode is exposed, and the electrodes are far apart, the electric field will appear similar to that of an electric field applied between two spherical electrodes. However, for longer electrode exposure lengths, the area between the electrodes will begin to more closely resemble Fig. 3.5 and have a larger ablation zone in the direction parallel to the length of the electrodes.

3.4.2.5 Electrode Arrays and Pulse Sequences

It is possible to use multiple electrodes positioned in an array to perform IRE focal ablation [7]. By grounding one (or multiple) electrode, and energizing another, an electric field is generated inside the target tissue, as in the case of two-needle electrode. Electrical pulses are often applied between each adjacent electrode combination to ablate a larger volume of tissue, but it is important to consider the consequences of these serial pulsing combinations, such as the one shown in Fig. 3.12a. Realizing that the tissue conductivity is dynamic and dependent on the local electric field intensity and temperature, it becomes clear that if a region of tissue has been electroporated previously, it will not have the same electrical properties with additional exposure. Indeed, additional electrical pulses delivered to the tissue will depend on the previous electrified state of the tissue. Figure 3.12b shows a cross-section of the electric field intensity and temperature distributions in simulated liver tissue with steady conductivity ($\sigma = 0.5$ S/m) and dynamic conductivity given by Sect. 4.2.1. Considering the more realistic case of dynamic conductivity, the electric field is distorted from what is predicted from simple models, and the
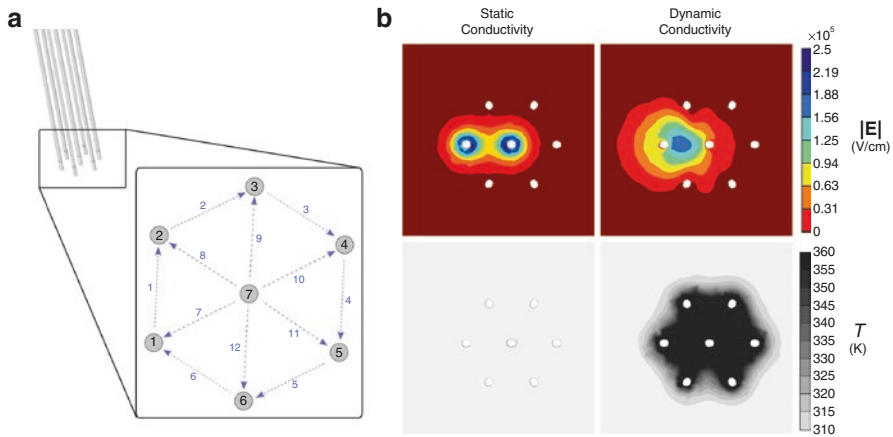
Fig. 3.12 The electric field and temperature distributions generated within a tissue during electroporation change the tissue conductivity and therefore depend on the tissue's pervious electric field exposure and temperature. A pulsing scheme for a 7-electrode array (*blue*) generates electric fields between every combination of two electrodes in the typical circular electrode array shown (1 cm between electrodes). The electric field and temperature distributions are shown at the completion of each serial pulsing step

temperature has risen dramatically beyond what the static model predicts. In order to induce minimal thermal damage during treatment, it is imperative that the dynamic response of a tissue to an electric field be considered during treatment planning and application.

Conclusion

An intuitive understanding of how electric fields behave in biological tissue involves understanding how electric fields are distributed within a tissue, impact the constituent cells within that tissue, and abstract that cellular impact back to measurable tissue-level properties. An understanding of these properties results in more accurate treatment planning prior to treatment and better clinical response to any intraoperative complications. IRE treatment is a complex, multi-scale, biophysical treatment modality that, when its biophysical mechanisms are appreciated and it is implemented in a well-considered manner, has been shown to provide clinically viable treatment options for patients that would otherwise not exist.

References

1. Abidor I, Arakelyan V, Chernomordik L, Chizmadzhev Y, Pastushenko V, Tarasevich M. 246 – electric breakdown of bilayer lipid membranes I. The main experimental facts and their qualitative discussion. Bioelectrochem Bioenerg. 1979;6(1):37–52.
2. Al-Sakere B, André F, Bernat C, Connault E, Opolon P, Davalos RV, Rubinsky B, Mir LM. Tumor ablation with irreversible electroporation. PLoS One. 2007;2(11):e1135.

3. Alberts B. Molecular biology of the cell. 4th ed. New York: Garland Science; 2002.

4. Bergman TL, Incropera FP, Lavine AS. Fundamentals of heat and mass transfer. Hoboken: Wiley; 2011.

5. Bhonsle SP, Arena CB, Sweeney DC, Davalos RV. Mitigation of impedance changes due to electroporation therapy using bursts of high-frequency bipolar pulses. Biomed Eng Online. 2015;14(Suppl 3):S3.

6. Buchner R, Hefter GT, May PM. Dielectric relaxation of aqueous NaCl solutions. Chem Eur J. 1999;103(1):1–9.

7. Campana LG, Cesari M, Dughiero F, Forzan M, Rastrelli M, Rossi CR, Sieni E, Tosi AL. Electrical resistance of human soft tissue sarcomas: an ex vivo study on surgical specimens. Med Biol Eng Comput 2016;54.5:773–87.

8. Čemažar J, Douglas TA, Schmelz EM, Davalos RV. Enhanced contactless dielectrophoresis enrichment and isolation platform via cell-scale microstructures. Biomicrofluidics. 2016;10(1):014109.

9. Corović S, Pavlin M, Miklavcic D. Analytical and numerical quantification and comparison of the local electric field in the tissue for different electrode configurations. Biomed Eng Online. 2007;6:37.

10. Davalos R, Rubinsky B, Mir L. Theoretical analysis of the thermal effects during in vivo tissue electroporation. Bioelectrochemistry. 2003;61(1–2):99–107.

11. R. V. Davalos, S. Bhonsle, R. E. Neal. Implications and considerations of thermal effects when applying irreversible electroporation tissue ablation therapy. Prostate. 2015;1118(Jan):n/a–n/a.

12. Davalos RV, Mir LM, Rubinsky B. Tissue ablation with irreversible electroporation. Ann Biomed Eng. 2005;33(2):223–31.

13. DeBruin KA, Krassowska W. Modeling electroporation in a single cell. I. Effects of field strength and rest potential. Biophys J. 1999;77(3):1213–24.

14. Dev SB, Dhar D, Krassowska W. Electric field of a six-needle Array electrode used in drug and DNA delivery in vivo: analytical versus numerical solution. IEEE Trans Biomed Eng. 2003;50(11):1296–300.

15. Dunki-Jacobs EM, Philips P, Martin RCG. Evaluation of resistance as a measure of successful tumor ablation during irreversible electroporation of the pancreas. J Am Coll Surg. 2014;218(2):179–87.

16. Edd JF, Davalos RV. Mathematical modeling of irreversible electroporation for treatment planning. Technol Cancer Res Treat. 2007;6(4):275–86.

17. Gabriel S, Lau R, Gabriel C. The dielectric properties of biological tissues: II. Measurements in the frequency range 10 Hz to 20 GHz. Phys Med Biol. 1996;41:2251.

18. Garcia P, Rossmeisl J, Neal REI, Ellis T, Davalos R. A parametric study delineating irreversible electroporation from thermal damage based on a minimally invasive intracranial procedure. Biomedica. 2011;10:34.

19. Gascoyne PRC, Pethig R, Burt JPH, Becker FF. Membrane changes accompanying the induced differentiation of friend murine erythroleukemia cells studies by dielectrophoresis. Biochim Biophys Acta Biomembr. 1993;1149(1):119–26.

20. Glaser RW, Leikin SL, Chernomordik LV, Pastushenko VF, Sokirko AI. Reversible electrical breakdown of lipid bilayers: formation and evolution of pores. Biochim Biophys Acta. 1988;940:275–87.

21. Hölzel R, Lamprecht I. Dielectric properties of yeast cells as determined by electrorotation. Biochim Biophys Acta Biomembr. 1992;1104(1):195–200.

22. Hu Q, Joshi RP, Beskok A. Model study of electroporation effects on the dielectrophoretic response of spheroidal cells. J Appl Phys. 2009;106(2):024701.

23. Ivorra A, Villemejane J, Mir LM. Electrical modeling of the influence of medium conductivity on electroporation. Phys Chem Chem Phys: PCCP. 2010;12(34):10055–64.

24. Kashchiev D, Exerowa D. Bilayer lipid membrane permeation and rupture due to hole formation. Biochim Biophys Acta. 1983;732(1):133–45.

25. Kotnik T, Bobanovic F, Miklavcic D. Applied electric fields-a theoretical analysis. Bioelectrochem Bioenerg. 1997;43:285–91.

26. Kotnik T, Miklavcic D. Analytical description of transmembrane voltage induced by electric fields on spheroidal cells. Biophys J. 2000;79(2):670–9.
27. Kranjc M, Bajd F, Sersa I, Woo EJ, Miklavcic D. Ex vivo and in silico feasibility study of monitoring electric field distribution in tissue during electroporation based treatments. PLoS One. 2012;7(9):3–10.
28. Mahnic-Kalamiza S, Kotnik T, Miklavcic D. Educational application for visualization and analysis of electric field strength in multiple electrode electroporation. BMC Med Educ. 2012;12:102.
29. Marcelja S. Structural contribution to solute-solute interaction. Croat Chem Acta. 1977;49(2):347–58.
30. Marcelja S, Radic N. Repulsion of interfaces due to boundary water. Chem Phys Lett. 1976;42(1):129–30.
31. Martin RCG, Kwon D, Chalikonda S, Sellers M, Kotz E, Scoggins C, McMasters KM, Watkins K. Treatment of 200 locally advanced (stage III) pancreatic adenocarcinoma patients with irreversible electroporation. Ann Surg. 2015;262(3):486–94.
32. Maxwell JC. A dynamical theory of the electromagnetic field. Philos Trans R Soc Lond. 1865;155(0):459–512.
33. Melenhorst MCAM, Scheffer HJ, Vroomen LGPH, Kazemier G, van den Tol MP, Meijerink MR. Percutaneous irreversible electroporation of unresectable hilar cholangiocarcinoma (Klatskin tumor): a case report. Cardio Vasc Interv Radiol. 2016;39(1):117–21.
34. Neal RE, Garcia PA, Robertson JL, Davalos RV. Experimental characterization and numerical modeling of tissue electrical conductivity during pulsed electric fields for irreversible electroporation treatment planning. IEEE Trans Biomed Eng. 2012;59(4):1076–85.
35. Neal RE, Millar JL, Kavnoudias H, Royce P, Rosenfeldt F, Pham A, Smith R, Davalos RV, Thomson KR. In vivo characterization and numerical simulation of prostate properties for non-thermal irreversible electroporation ablation. Prostate. 2014;74:458–68.
36. Neff HP. Introductory electromagnetics. New York: Wiley; 1991.
37. Pavlin M, Kanduser M, Rebersek M, Pucihar G, Hart FX, Magjarevic R, Miklavcic D. Effect of cell electroporation on the conductivity of a cell suspension. Biophys J. 2005;88(6):4378–90.
38. Powell KT, Weaver JC. Transient aqueous pores in bilayer membranes: a statistical theory. Bioelectrochem Bioenerg. 1986;211:211–27.
39. Rols MP, Teissie J. Modulation of electrically induced permeabilization and fusion of Chinese hamster ovary cells by osmotic pressure. Biochemistry. 1990;29(19):4561–7.
40. Scheffer HJ, Vogel JA, van den Bos W, Neal RE, van Lienden KP, Besselink MGH, van Gemert MJC, van der Geld CWM, Meijerink MR, Klaessens JH, Verdaasdonk RM. The influence of a metal stent on the distribution of thermal energy during irreversible electroporation. PLoS One. 2016;11(2):e0148457.
41. Schwan H. P. Electrical properties of tissue and cell suspensions. In: Advances in biological and medical physics, Vol. 5. New York: Academic; 1957. p. 147.
42. Wendler JJ, Fischbach K, Ricke J, Jürgens J, Fischbach F, Köllermann J, Porsch M, Baumunk D, Schostak M, Liehr U-b, Pech M. Irreversible electroporation (IRE): standardization of terminology and reporting criteria for analysis and comparison. Pol J Radiol. 2016;81:54–64.